Computers and Concrete, *Vol. 16, No.* 6 *(2015) 933-962*
DOI: http://dx.doi.org/10.12989/cac.2015.16.6.933

Application of a mesh-free method to modelling brittle fracture and fragmentation of a concrete column during projectile impact

Raj Das*[1] and Paul W. Cleary[2]

[1] *Department of Mechanical Engineering, University of Auckland, Auckland 1010, New Zealand*
[2] *CSIRO Mathematics, Informatics and Statistics, Clayton, Victoria 3168, Australia*

(*Received August 8, 2014, Revised November 6, 2015, Accepted November 9, 2015*)

Abstract. Damage by high-speed impact fracture is a dominant mode of failure in several applications of concrete structures. Numerical modelling can play a crucial role in understanding and predicting complex fracture processes. The commonly used mesh-based Finite Element Method has difficulties in accurately modelling the high deformation and disintegration associated with fracture, as this often distorts the mesh. Even with careful re-meshing FEM often fails to handle extreme deformations and results in poor accuracy. Moreover, simulating the mechanism of fragmentation requires detachment of elements along their boundaries, and this needs a fine mesh to allow the natural propagation of damage/cracks. Smoothed Particle Hydrodynamics (SPH) is an alternative particle based (mesh-less) Lagrangian method that is particularly suitable for analysing fracture because of its capability to model large deformation and to track free surfaces generated due to fracturing. Here we demonstrate the capabilities of SPH for predicting brittle fracture by studying a slender concrete structure (column) under the impact of a high-speed projectile. To explore the effect of the projectile material behaviour on the fracture process, the projectile is assumed to be either perfectly-elastic or elastoplastic in two separate cases. The transient stress field and the resulting evolution of damage under impact are investigated. The nature of the collision and the constitutive behaviour are found to considerably affect the fracture process for the structure including the crack propagation rates, and the size and motion of the fragments. The progress of fracture is tracked by measuring the average damage level of the structure and the extent of energy dissipation, which depend strongly on the type of collision. The effect of fracture property (failure strain) of the concrete due to its various compositions is found to have a profound effect on the damage and fragmentation pattern of the structure.

Keywords: mesh-free method; smoothed particle hydrodynamics; concrete; fracture; impact

1. Introduction

Fracture and fragmentation are complex phenomena, involving multiple physical processes occurring at different time and spatial scales. The sources of fracture are initial flaws, micro-structural defects, micro and macro voids (Davison and Stevens 1973, Shockey *et al*. 1974). Fracture failure plays a significant role in a wide range of systems and processes. For example, the prediction of the characteristics of fracture failure under impact and shock wave loading, and the

*Corresponding author, Ph.D., E-mail: r.das@auckland.ac.nz

http://www.techno-press.org/?journal=cac&subpage=8 ISSN: 1598-8198 (Print), 1598-818X (Online)

properties of the resulting fragments provide key inputs in setting up controlled blasts in mines (Mitchell 1993, Kleine *et al*. 1997, Fang and Harrison 2001). Modelling breakage in granular flows is useful in optimising the design and setting operating parameters in mills to enhance mill efficiency and achieve desired product quality (Morrison and Cleary 2004). The assessment of the extent of damage and evaluation of possible preventive measures assume importance in heavy capital intensive industries, such as mining (Tait and Emslie 2005, Wen *et al*. 2005), aircraft (Fujiwara 1994, Wang *et al*. 1997, Ju *et al*. 2007), and rail (Sharir *et al*. 1982, Mok *et al*. 2007), where failure by fracture can lead to performance degradation, reduction in operational life, and even catastrophic failure of a system. Fracture resistant designs and regular monitoring of the health (damage conditions) of a system can lead to significant savings in maintenance and downtime costs (Uetani and Tagawa 1999, Takabatake *et al*. 2005). Recently, it has also been used to explore the breakdown of elastoplastic and elastic-brittle foodstuffs in the oral cavity during chewing (Harrison and Cleary 2014).

Fracture and fragmentation of concrete is an important aspect in many applications, in particular for civil infrastructures. Several past researches have focused on numerical and experimental studies involving both quasi-static and dynamic fracture of concrete (Kumar and Barai 2010, Hu *et al*. 2015, Huang *et al*. 2015, Rezaie and Farnam 2015, Selman *et al*. 2015, Skarżyński *et al*. 2015). High temperatures and loading rate can affect the fracture properties, such as softening behaviour and fracture toughness of concrete (Hu *et al*. 2015, Yu *et al*. 2015, Skarżyński *et al*. 2015) have applied numerical methods (FEM and DEM) for modelling fracture, considering the internal structure of concrete explicitly using X-ray tomography and μCT images (Huang *et al*. 2015, Skarżyński *et al*. 2015). A two-dimensional meso-scale model of fracture of concrete beams under quasi-static loading (three-point bending tests) was performed to demonstrate this (Skarżyński *et al*. 2015). Impact fracture behaviour of carbon nanotube reinforced concrete was studied by applying multiscale dynamic fracture model (Eftekhari and Mohammadi 2015).

In the past, approaches for studying fracture have been heavily dependent on empirical relations based on laboratory scale experimental data (Fujiwara 1989). For large scale impact problems, the extrapolation of this data using a scaling law is not always reliable (Shockey *et al*. 1974). As a result, the empirical models do not often perform well outside the regimes of the original experiments. Numerical fracture models, based on well-reasoned physical models, can potentially provide effective solutions for predicting large scale fracturing events, such as explosions in mines (Napier 1990), the formation of impact craters (Melosh and Collins 2005), and the fragmentation of asteroids (Melosh 1985, Fujiwara 1989). Furthermore, the assessment of damage initiation and progression can be rapidly and easily performed for a wide range of problem parameters, such as geometry, loading, initial defect characteristics and distribution, which may extend beyond the scope of experiments used to generate the model. Modelling can also assist in designing and planning new experiments (Pierazzo and Melosh 2000). Effective damage modelling techniques in conjunction with efficient numerical methods have strong potential for increasing our understanding of fundamentals of breakage in many applications and for providing practical tools that can be used for equipment and structure design.

Here we use a particle based method called Smoothed Particle Hydrodynamics (SPH) to model brittle failure of structures under impact load. SPH was first proposed by (Gingold and Monaghan 1977 and Lucy 1977) for astrophysical problems. It has been traditionally used for modelling fluid flows (Monaghan 1992, 1994, Cleary *et al*. 2002, Imaeda and Inutsuka 2002, Kulasegaram *et al*. 2003, Cedric *et al*. 2005, Cleary *et al*. 2006a/b, Fang *et al*. 2006, Cleary *et al*. 2007) and thermal problems (Cleary 1998, Cleary and Monaghan 1999). In recent years, there has been a growing interest in applying SPH to a wide variety of solid mechanics problems (Libersky and Petschek 1990, Wingate and Fisher 1993, Gray *et al*. 2001, Gray and Monaghan 2004, Liu *et al*. 2004, Cleary *et al*. 2006a/b, Cleary and Das 2008, Cleary 2010a/b, Cleary *et al*. 2012, Das and Cleary 2013). SPH is a broadly established mesh-free numerical method, which is used to obtain solutions to systems of partial differential equations. The problem geometry is discretised into 'particles' that represent specific material volumes. For details of SPH fundamentals, see (Monaghan 1992, 2005, Cleary *et al*. 2007).

A particle method (such as SPH) is preferred over traditional mesh-based techniques (such as FEM and BEM) for such fracture prediction problems for several reasons. Firstly the grid based methods require very fine meshes to model the theoretically singular stress field in the neighbourhood of damage locations (e.g., crack tips) (Aliabadi and Rooke 1991). As the damage propagates, the structure then needs to be re-meshed to take into account the localised change in geometry in order to avoid accuracy and stability issues relating to poor element quality after large deformation. Automated re-meshing can lead to mesh distortion, numerical diffusion and inaccurate results, especially in gradient computations (Fernandez-Mendez *et al*. 2005), and can be computationally expensive. A primary advantage of SPH for fracture is that as a particle based technique it does not have any underlying grid structure to represent the problem geometry and so avoids the inaccuracies and instabilities associated with maintaining the integrity and quality of the mesh during large deformation. The mesh-free nature of SPH makes it ideally suited to modelling processes that involve extreme deformations and discontinuities, such as fracture and fragmentation, material processing, and a broad range of geomechanics problems (Karekal *et al*. 2011, Das and Cleary 2013). Its grid-free nature enables the fracturing process and the associated change in structural configuration to be naturally handled without the need to re-mesh.

One specific requirement of fracture simulation is to be able to model the disintegration of solids to produce fragments. A common approach is to explicitly simulate crack propagation with FEM by detaching elements along the sides of propagating cracks, which is accomplished by allowing the separation of the coincident (shared) nodes of the adjacent elements as the fracture surface evolves (Aliabadi and Rooke 1991). This also requires a very fine mesh to allow the propagation of damage/cracks to be accurately predicted and avoid mesh dependent fracture pathways. When using a discrete method, such as bonded DEM (Potyondy and Cundall 2004), fracturing is simulated by rupturing the bonds between adjacent particles. This also leads to dependency of fracture patterns on particle configurations (size, shape and pattern of arrangement). Also DEM is primarily suitable for granular/particulate material fracture and cannot be used for applications involving large scale fracture of continuum materials. A continuum volume averaged representation of damage means that the cracks are not constrained to propagate along specific element boundaries even for a coarse mesh allowing the natural development of fracture patterns. SPH has the ability to naturally track new free surfaces as they are generated during fracture.

SPH is a Lagrangian method, in which the equations are solved on the particles which are fully advected with the material velocities. This eliminates the non-linear advection term from the momentum equation which normally creates significant diffusion errors for high speed deformation. SPH is able to follow high deformation and structural motion without the need to include any explicit free surface tracking, and is therefore much less diffusive. With the use of a Lagrangian reference frame, each particle continuously represents the same volume of material. This provides a natural ability to track material history and history dependent properties of the material (Cleary *et al*. 2007, Cleary 2010a/b, Cleary *et al*. 2012). This includes the extent of damage, plastic strain, surface oxide formation, material composition and phase change. SPH has been successfully applied to simulate different types of solid material forming processes (Cleary *et al*. 2006a/b) using such history tracking capabilities. In general, fracturing is driven by the stress-strain history experienced by the material. Traditional Eulerian methods have difficulties in tracking the stress-strain history on a node by node basis and in predicting the evolution of damage in the specimen. Fahrenthold and Yew (Fahrenthold and Yew 1995) incorporated the Grady-Kipp fracture model in an Eulerian code and applied the fracture-fragmentation theory for studying orbital debris shield impact problems. They reported difficulties in modelling the fracture and tracking the evolution of the resulting fragments (debris) in the Eulerian framework. The history tracking ability of SPH provides a natural framework enabling the prediction of damage initiation and crack propagation. The dynamics of damage evolution is then able to be explicitly included in the analysis.

In this paper, the advantages of the SPH method for impact fracture problems is demonstrated by applying it to model brittle fracture of a slender concrete column under the high-speed impact by a projectile. Brittle fracture of slender structures under impact has importance in many applications, such as high-speed weapons systems (e.g., missiles, torpedoes etc.), impact resistant buildings, structures on gas and petroleum wells, and extreme geophysical events. This simplified example can help understand the significant phenomena of interest and provide insights into the key mechanisms of fracture and the resulting distribution of the fragments for similar categories of collision problems. The stress field and the resulting damage in the structure are studied using a continuum damage model implemented in SPH. The effect of the constitutive property of the projectile (perfectly-elastic or elastoplastic) on the fracture pattern, fragmentation and energy transfer is examined and shown to be extremely important in controlling the rate of energy transfer from the projectile to the target and its resulting fracture behaviour. The effect of the fracture property (failure strain) of the concrete is also evaluated, and the failure strain is shown to have a crucial role in determining the dynamic fracture behaviour.

2. Smoothed Particle Hydrodynamics (SPH) method

The Smoothed Particle Hydrodynamics (SPH) method is a continuum numerical method, in which a physical object is analysed by representing it with a set of particles. These particles move according to the governing differential equations and are assigned individual material properties. Continuous field variables (functions) at a given particle are approximated using local interpolations on surrounding particles to construct their distributions over the entire volume of material. This is a spatial discretisation of the governing partial differential equations. The interpolated value of a field variable A at any position $\mathbf{r}$ can be expressed using SPH interpolation as (Monaghan 1992)

$$A(\mathbf{r}) = \sum_b m_b \frac{A_b}{\rho_b} W(\mathbf{r}-\mathbf{r}_b, h) \tag{1}$$

where m_b and ρ_b are the mass and the density of particle b located at $\mathbf{r}_b$, h is the smoothing length, and the sum is over all particles b within a radius $2h$ of the point at $\mathbf{r}$. Here $W(\mathbf{r} - \mathbf{r}_b, h)$ is a C^2 spline based interpolation or smoothing kernel with radius $2h$ which approximates the shape of a Gaussian function, but has compact support.

The gradient of field variable A can be obtained by differentiating the interpolation Eq. (1) to give

$$\nabla A(\mathbf{r}) = \sum_b m_b \frac{A_b}{\rho_b} \nabla W(\mathbf{r} - \mathbf{r}_b, h) \tag{2}$$

Using these interpolations for second and first order spatial derivatives, parabolic partial differential equations can be converted into ordinary differential equations containing time derivatives for the motion of the particles and the rates of change of the associated field variables. Suitable finite difference methods can then be used to numerically solve the resultant differential equations. The differential equations governing the structural responses and their SPH approximations will be presented below.

2.1 Continuity equation

The continuity equation for an elastoplastic solid is given as

$$\frac{d\rho}{dt} = -\rho \nabla \bullet \mathbf{v} \tag{3}$$

where ρ is the density and $\mathbf{v}$ is the velocity. For use in the SPH form, the position vector of particle a relative to particle b is denoted by $\mathbf{r}_{ab} = \mathbf{r}_a - \mathbf{r}_b$, and $W_{ab} = W(\mathbf{r}_{ab}, h)$ is the interpolation kernel with smoothing length h evaluated for the distance $|\mathbf{r}_{ab}|$. An SPH discretisation of the continuity equation suitable for materials with free surfaces is given by

$$\frac{d\rho_a}{dt} = \sum_b m_b (\mathbf{v}_a - \mathbf{v}_b) \bullet \nabla W_{ab} \tag{4}$$

where ρ_a is the density of particle a with velocity $\mathbf{v}_a$, and m_b is the mass of particle b with velocity $\mathbf{v}_b$. This form of the continuity equation is Galilean invariant (as the positions and velocities appear as differences), has good numerical conservation properties, and is not affected by density discontinuities or free surfaces.

2.2 Momentum equation

The momentum equation used for the elastic deformation of solids is

$$\frac{d\mathbf{v}}{dt} = \frac{1}{\rho} \nabla \bullet \boldsymbol{\sigma} + \mathbf{g} \tag{5}$$

where $\boldsymbol{\sigma}$ is the stress tensor, and $\mathbf{g}$ is the body force.

The momentum Eq. (5) can be discretised using SPH interpolation as

$$\frac{d\mathbf{v}_a}{dt} = \sum_b m_b \left(\frac{\boldsymbol{\sigma}_a}{\rho_a^2} + \frac{\boldsymbol{\sigma}_b}{\rho_b^2} + \Pi_{ab} \mathbf{I} \right) \bullet \nabla_a W_{ab} + \mathbf{g}_a \tag{6}$$

where $\boldsymbol{\sigma}_a$ and $\boldsymbol{\sigma}_b$ are the stress tensors of particles a and b, $\mathbf{g}_\mathbf{a}$ is the body force at particle a, and

Π_{ab} is a term that produces a shear and bulk viscosity (Gray *et al*. 2001).

The stress tensor can be written as

$$\boldsymbol{\sigma} = -P\mathbf{I} + \mathbf{S} \tag{7}$$

where P is the pressure and **S** is the deviatoric stress tensor.

Assuming linear elastic material response conforming to Hooke's law, the evolution equation for the components of the deviatoric stress **S** is computed using the Jaumann rate equation accounting for large rotational effects (Gray *et al*. 2001)

$$\frac{dS^{ij}}{dt} = 2G\left(\dot{\varepsilon}^{ij} - \frac{1}{3}\delta^{ij}\dot{\varepsilon}^{ij}\right) + S^{ik}\Omega^{kj} + \Omega^{ik}S^{kj} \tag{8}$$

where G is the shear modulus, and the components of the strain rates $\dot{\varepsilon}^{ij}$ are given by

$$\dot{\varepsilon}^{ij} = \frac{1}{2}\left(\frac{\partial v^i}{\partial x^j} + \frac{\partial v^j}{\partial x^i}\right) \tag{9}$$

and Ω^{ij} is the rotation tensor and is given by

$$\Omega^{ij} = \frac{1}{2}\left(\frac{\partial v^i}{\partial x^j} - \frac{\partial v^j}{\partial x^i}\right) \tag{10}$$

The SPH equations for the strain rate $\dot{\varepsilon}_a$ and the Jaumann rotation tensor Ω_a for particle a are

$$\dot{\varepsilon}^{ij}_a = \frac{1}{2}\sum_b \frac{m_b}{\rho_b}[(v_b^i - v_a^i)\frac{\partial W_{ab}}{\partial x_a^j} + (v_b^j - v_a^j)\frac{\partial W_{ab}}{\partial x_a^i}] \tag{11}$$

$$\Omega^{ij}_a = \frac{1}{2}\sum_b \frac{m_b}{\rho_b}[(v_b^i - v_a^i)\frac{\partial W_{ab}}{\partial x_a^j} - (v_b^j - v_a^j)\frac{\partial W_{ab}}{\partial x_a^i}] \tag{12}$$

2.3 Equation of state

The SPH method used here is fully transient and resolves the stress waves propagating through the solid materials. The pressure-density relationship is described by the equation of state

$$P = c^2(\rho - \rho_0) \tag{13}$$

where ρ_0 is the reference density, ρ is the current density and c is the speed of sound in the solid material. The sound speed c is given from the material bulk modulus and density by $c = \sqrt{\frac{K}{\rho_0}}$.

The Poisson ratio is $\eta = \frac{(3K/G - 2)}{2(3K/G + 1)}$.

When modelling fluid flow problems with SPH, the sound speed is often treated as a numerical parameter and is chosen in such a way so as to artificially increase compressibility. This allows the inherently compressible form of the SPH formulation to be applied to essentially incompressible (weekly compressible) fluids with significant increase in the computational speed. It should be noted that unlike this approach for fluids, for solid deformation problems the real speed of sound for each material is used in order to ensure that the controlling stress waves are fully resolved.

The Improved Euler scheme given in (Monaghan 2005) was used for explicit integration of the SPH equations. For elastic solids, the maximum time step Δt_s is

$$\Delta t_s = \min_a \{0.5h/c_a\} \tag{14}$$

where c_a is the speed of sound for the material of particle *a*.

The tensile instability correction and the artificial viscosity described in (Gray *et al*. 2001) are also used. The tensile instability correction coefficient used was 0.1, and the artificial viscosity used was 1.0 (Das and Cleary 2006).

2.4 Von mises plasticity with linear isotropic hardening

The radial return plasticity model of (Wilkins 1964) is used to model elastoplastic deformation of the projectile. This has been used successfully to model forging (Cleary *et al*. 2012), elastoplastic impact (Cleary 2010a/b), welding (Das and Cleary 2015a/b), metal extrusion (Prakash and Cleary 2015), and other severe plastic deformation process (Fagan *et al*. 2012). Other plasticity models can also be used in this framework. A trial deviatoric stress $\mathbf{S_{tr}}$ is calculated assuming an initial elastic response. The increment of plastic strain is

$$\Delta\varepsilon^p = \frac{\sigma_{vm} - \sigma_y}{3G + H} \tag{15}$$

where σ_{vm} is the von Mises stress and σ_y is the current yield strength. The plastic strain is then incremented

$$\varepsilon^p = \varepsilon^p + \Delta\varepsilon^p \tag{16}$$

The yield strength increment $\Delta\sigma_y$ at each time step is calculated as

$$\Delta\sigma_y = H\,\Delta\varepsilon^p \tag{17}$$

where *H* is the hardening modulus. The deviatoric stress **S** at the end of a time step is given by

$$\mathbf{S} = \mathrm{r}_s\mathbf{S_{tr}} \tag{18}$$

where r_s is the radial scale factor given by

$$r_s = \sigma_y / \sigma_{vm} \tag{19}$$

2.5 Stabilisation method: tensile instability correction

SPH may show instabilities for solid deformation of materials under tension. The origin of ‘so called' tensile instability has received much attention in SPH. It can affect the solution of solid deformation problems by producing non-physical clustering of particles in the zone of material under tension, leading to erroneous numerical fracture. The tensile instability in SPH was first studied by Swegle *et al*. (Swegle *et al*. 1995). We use the 'principal stress correction' approach proposed by Monaghan (Monaghan 2000) and subsequently extended for solids by Gray *et al*. (Gray *et al*. 2001) to counteract this. This method has been shown to be robust for solid deformation problems (Libersky and Petschek 1990, Wingate and Fisher 1993, Gray *et al*. 2001, Gray and Monaghan 2004, Liu *et al*. 2004, Cleary *et al*. 2006a,b). Das and Cleary have performed a detailed study of the effect of this tensile instability correction factor on the accuracy of the SPH stress solution for elastic deformation under uniaxial loading (Das and Cleary 2015a).

The 'principal stress correction' method involves the addition of a correcting artificial stress to the tensile (positive) principal stress components. The form of the artificial stress is based on a linear perturbation analysis of the governing partial differential equations. The calculation of the artificial stress involves a scaling parameter ψ termed as the 'tensile coefficient', which controls the magnitude of the artificial stress and controls the numerical instability (for further details refer to (Gray *et al*. 2001)). A value of ψ in the range of 0.1-0.2 was found to be suitable for the present study. Implementation of tensile instability correction involves modifying the momentum Eq. (6) by adding the artificial stress terms as

$$\frac{d\mathbf{v}_a}{dt} = \sum_b m_b \left(\frac{\boldsymbol{\sigma}_a}{\rho_a^2} + \frac{\boldsymbol{\sigma}_b}{\rho_b^2} + \Pi_{ab}\mathbf{I} + (\mathbf{R}_a + \mathbf{R}_b) f_{ab}^n \right) \bullet \nabla_a W_{ab} + \mathbf{g} \tag{20}$$

where $\mathbf{R_a}$ and $\mathbf{R_b}$ are the artificial stress tensors of particles a and b in the world co-ordinate frame, $f_{ab} = W(r_{ab})/W(\Delta p)$, where Δp is the SPH particle spacing, n is an index with an optimum value of 4.0 (Gray *et al*. 2001) that ensures the effect of the artificial stress is limited to the nearest neighbouring particles.

3. Accuracy of SPH for solid deformation problems and its use for concrete

The accuracy of the mesh-free SPH method has been evaluated by many researchers (as mentioned below), including the present authors (Das and Cleary 2010, Das and Cleary 2015a). The accuracy of different SPH formulations and/or stabilisation schemes for elastic solids has been assessed by comparing displacement, velocity, or stress with a reference solution. The variation of these field variables over space (the problem domain) or with time at some specific points were compared with the reference solution. In general, displacement and velocity are found to agree well with the reference solutions. Early verification or validation of the SPH method was carried out using typical 1D stress wave solutions in elastic bars/rods obtained using analytical or finite element methods, see (Dyka and Ingel 1995, Liu *et al.* 1995, Dyka *et al*. 1997, Chen *et al*. 1999, Randles and Libersky 2000, Vignjevic *et al*. 2000, Bonet and Kulasegaram 2001, Vidal *et al*. 2007). Several researchers have established the accuracy of SPH for collision and impact problems (Randles and Libersky 2000, Vignjevic *et al*. 2000). Randles and Libersky (2000) considered high-speed impact of an aluminium rod with an aluminium substrate, which is in contact with a copper plate beneath it. They studied propagation of shock waves across the material (Al-Cu) interface using SPH, and the solutions compared well with the analytical results. Vignjevic and co-workers studied collisions between elastic aluminium cylindrical bars, elastoplastic steel blocks and rubber rings (Vignjevic *et al*. 2000). The solutions showed reasonable agreement with the explicit FE solutions using LS-DYNA. Lemiale and co-workers considered high speed collision of a spherical metallic particle with a metal substrate. After accounting for the very high strain rate effects in the material model, a good agreement was obtained with the experiment (Lemiale *et al*. 2014). Das and Cleary demonstrated the accuracy and convergence of SPH for uniaxial compression problems (Das and Cleary 2015a). They also showed good agreement between the SPH predicted fracture pattern in an UCS test with the experimental one (Das and Cleary 2010). The SPH method has been established as a reliable method for solid deformation problems, particularly for high-speed impact applications that involve large-scale, discontinuous deformations, including fractures and fragmentations. Hence, the SPH method has been adopted in this work.

4. Damage modelling implementation in SPH

The SPH formulation for elastic solid deformation (Gray *et al*. 2001) is combined with a continuum damage model (Das and Cleary 2010) to simulate fracture in concrete structures subjected to impact. A modified form of the Grady-Kipp damage model (Grady and Kipp 1980, Das and Cleary 2010), as proposed by Melosh *et al*. (Melosh *et al*. 1992), forms the basis of fracture modelling in this study. This model by Melosh *et al*. (Melosh *et al*. 1992) was further extended by Das and Cleary (2010) and Karekal *et al*. (2011) for geomechanical fracture initiation and propagation in rocks. It allows prediction of damage based on the local stress history and flaw distribution. This damage model was applied to earthquake response analysis of Koyna dam and showed good agreement with experimental and field observations (Das and Cleary 2013). This damage model presented below will be used here to model fracturing of concrete caused by high-speed projectile impact.

The key issues in the numerical modelling of brittle damage are: representing inherent initial defects and cracks, characterising the level of fracture in terms of strengths of joints and faults, and representing damage growth leading to fracture and fragmentation. In the context of SPH implementation, a scalar damage parameter D characterises the volume-averaged micro-fracture of the material volume represented by each SPH particle. The damage parameter is used to modify the stress tensor so as to inhibit the transmission of tensile stress between particles. The damage parameter lies between 0 and 1. Material with $D = 0$ is undamaged and is able to transmit the full tensile load, whereas material with $D = 1$ is fully damaged and cannot transmit any tensile load, which thus creates a partial macro crack. The damage parameter evolves based on the strain history of each particle, leading to dynamic fracture initiation and propagation. Contiguous cracked material represented by connected macro-cracks across a body leads to fragmentation. This type of model has been applied to the fracture studies of oil shale using a finite difference framework, and showed good agreement with the experimental data (Grady *et al*. 1980).

In the Grady-Kipp model, the assumption of a Weibull distribution for the flaws that act as nucleation sites for crack initiation leads to an integral equation in D (Grady and Kipp 1980), given by

$$D(t) = \frac{4}{3}\pi\, C_g^3 \int_0^t n'(\varepsilon)\,\dot{\varepsilon}\,(1-D)\,(t-\tau)^3\, d\tau \tag{21}$$

where C_g is the crack velocity which controls the rate of damage growth during dynamic fracture, ε

is the tensile strain, n' is the change in number of flaws due to crack initiation and growth, t is the time, τ is the past time, i.e., $(t- \tau)$ is the time interval. This model incorporates the effect of strain rate on the dynamic fracture due to the presence of strain rate in the integral Eq. (21).

An approximate differential form of the Grady-Kipp damage evolution model (Eq. (21)) is given as (Grady and Kipp 1980)

$$\frac{dD^{1/3}}{dt} = \frac{(m+3)}{3}\alpha^{1/3}\varepsilon^{m/3} \tag{22}$$

where α is a material constant calculated from three material fracture parameters k, m, and C_g

$$\alpha = \frac{8\pi C_g^3 k}{(m+1)(m+2)(m+3)} \tag{23}$$

In the approximate form Eq. (22), the effect of strain rate is taken into account by the crack velocity, C_g, during dynamic fracture. The original Grady-Kipp model was defined only for one dimensional plain strain problems. For two or three-dimensional problems, the full multi-component stress-strain field needs to be reduced to the one-dimensional analysis framework presented in (Grady and Kipp 1980). One method proposed in (Thorne *et al*. 1990) replaces the longitudinal strain in (Grady and Kipp 1980) by the volumetric strain (average of the three longitudinal strain components). This poses difficulties when some of the longitudinal strain components are compressive and some are tensile, and their magnitudes are such that the resulting volumetric strain is compressive. In this case, no damage evolution will occur under a compressive volume strain according to this damage model, but in practice damage accumulation should take place due to the tensile component(s) of the strain tensor. To avoid this, Melosh *et al*. (Melosh *et al*. 1992) introduced an effective tensile strain given by

$$\varepsilon = \sigma_{\max} / \left(K + \frac{4}{3}G\right) \tag{24}$$

where $\sigma_{\max}$ is the maximum positive (tensile) principal stress, and K is the bulk modulus of the material. Damage then accumulates when the effective strain exceeds a threshold value $\varepsilon_{\min}$

$$\varepsilon_{\min} = (Vk)^{-1/m} \tag{25}$$

where V is the volume of the SPH particle.

As proposed in (Das and Cleary 2010), this effective strain (Eq. (24)) is used in the evolution Eq. (22) to predict the damage state of the material. So for damage evolution in SPH, the combination of the differential version of the Grady-Kipp model (Eq. (22)) and the effective tensile strain (Eq. (24)) is used.

The method of application of damage variable to modify the stress tensor in momentum equation is also not unambiguous. A common approach has been to scale all components of the stress tensor by $(1 - D)$ (Melosh *et al*. 1992). This equally modifies both the compressive and tensile normal stresses, as well as the shear stresses. This does not properly account for the damage induced stress transfer process. The compressive stress components should not be reduced by the damage, because the material in a damaged region remains capable of transmitting forces under compression. It is only the tensile force transmission between adjacent particles that should be reduced. Another approach, proposed by Gray and Monaghan (Gray and Monaghan 2004), is not to scale all components of the deviatoric stress tensor by the damage, but to only scale the negative (tensile) pressure. Such approaches are based on ad hoc choices of which stress components the damage is applied. A better approach, proposed in (Das and Cleary 2010), is to rotate the total stress tensor into its principal co-ordinate frame where the tensile and compressive stresses are explicitly identified and then to scale only the tensile components of the principle stresses. The scaled stresses are then rotated back to the global co-ordinate frame to give the post-damage stresses used in the stress evolution and momentum equations. The Grady-Kipp damage model was modified in (Das and Cleary 2010) to incorporate this where the tensile components of the principal stresses for each SPH particle are scaled by its damage level to calculate the effective principal stress as

$$\begin{aligned} \sigma_d^i &= (1-D)\sigma_p^i \quad \text{if} \quad \sigma_p^i \geq 0 \\ \sigma_d^i &= \sigma_p^i \quad \text{if} \quad \sigma_p^i < 0 \end{aligned} \tag{26}$$

where σ^i_d and σ^i_p are the principal stresses for the damaged and undamaged material, respectively. The effective stress tensor at the global coordinate frame $\boldsymbol{\sigma}_\mathbf{e}$ is then computed by transforming the effective principal stress tensor $\boldsymbol{\sigma}_\mathbf{d}$ as

$$\boldsymbol{\sigma}_\mathrm{e} = \mathbf{T}\boldsymbol{\sigma}_\mathrm{d} \tag{27}$$

where **T** is the rotation matrix from the principal co-ordinate frame to the global frame.

5. Collision problem configuration

The collision of a high speed rectangular projectile with a stationary column to study the fracture initiation and propagation pattern using 2D SPH simulations is investigated. We consider two cases in which the projectile is either perfectly-elastic or elastoplastic in order to examine the effect of material constitutive behaviour on the impact fracture pattern.

Fig. 1 shows a schematic of the collision configuration in which the projectile travels from right to left with a velocity of 125 m/s and collides with the stationary column whose base is fixed. The column is 2 m wide and 10 m high and is made of concrete with bulk modulus 16.7 GPa, shear modulus 8.1 GPa and density 2300 kg/m^3. The Weibull damage parameters of the concrete are $k = 1.0 \times 10^{22}$ and $m = 9$ from Melosh *et al.* (Melosh *et al*. 1992). For the base case simulation, the threshold activation strain for damage growth is assumed to be 3.0×10^{-4} for the entire column. The projectile is made of steel with bulk modulus 184.2 GPa, shear modulus 80.2 GPa, and density 7800 kg/m^3. The projectile is assumed to be damage resistant and so deforms either elastically or elastoplastically. In the SPH models, the column and projectile were discretised with initially rectangular grid pattern of 0.05 m spacing, giving 16,004 and 6,442 particles respectively. Based on these material properties, the sound speeds were 2695 and 4860 m/s in the column and projectile respectively.

In the configuration being modelled, the normal forces at the impact locations are extremely high and cause the majority of the fracture and associated fragmentation, leading to the resultant highly accelerated motion of materials. There is little transverse motion during the contact phase and so the tangential contact forces are relatively small. The limiting friction in the tangential direction at the contact surfaces is very high because of the high normal loads. In contrast, the transverse (tangential) loads remain significantly lower than the normal loads, which rarely approach or exceed the frictional limit. On this basis an explicit contact friction model was not included in the current SPH formulation.

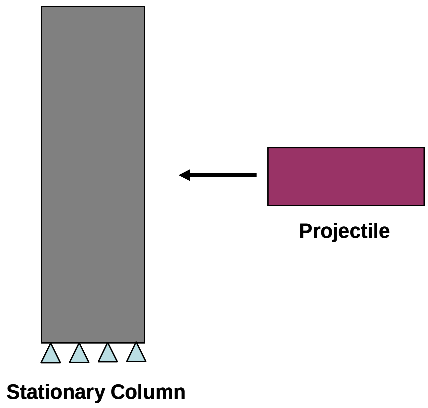

Fig. 1 Schematic of the projectile-column collision configuration

The tangential force at contacts is provided by the viscous stress term in the momentum Eq. (6). The absence of an explicit friction model could potentially lead to an over-estimation of the transverse motion. However, the simulation predictions, both at the early stage and during fracturing of the column, indicate that the transverse motion is indeed relatively small and that this assumption is reasonable.

Dynamic fracture of a brittle solid usually occurs in three stages, primary, secondary and tertiary (Das and Cleary 2010). Primary fracture is the major damage experienced in the early stages which predominantly contributes towards the catastrophic failure of a structure. It initiates from regions with very high stress concentrations. The cracks propagate over long distances, producing sharp fracture planes and causing a high level of damage. The secondary stage begins when additional damage or cracks are generated from either the primary fracture planes or from the initially highly damaged regions. These cracks propagate over shorter distances and produce localised debris or smaller fragments than those generated by primary fracturing. During secondary fracture the fragments remain within the original structure. Tertiary fracture is the localised fracture of fragments/debris due to collision with other fragments as they fly off. Since they are already partially damaged, they can easily undergo tertiary fracture.

The concrete in such an impact problem can be modelled by one of the two broad approaches, continuum or discrete methods:

In the continuum approach, such as the SPH method, the constituents of concrete, particularly the aggregate and cement, are represented as a continuous medium. Cracks are able to propagate through either the cement (surrounding the aggregate) or through the aggregates depending on their relative strengths and interface properties, thus allowing the fracturing of either or both the cement and aggregate. This is a key advantage of a continuum modelling approach. The SPH method has been used for modelling both the projectile and concrete in this workIn the discrete approach, such as the Discrete Element Method (DEM), whereby bonded rigid particles are used to represent the concrete (Potyondy and Cundall 2004), fracture is simulated by breakage of the bonds. With this method the deformation is restricted only to the bonds (representing the cement phase) while the aggregates are rigid and remain undeformed. Such DEM approaches may be suitable if the cement is less stiff (and so is the dominant contributor to the deformation) and weaker than the aggregate (so that the fracture is predominantly restricted to the cement phase rather than being within the aggregates). However, if the strength of the aggregates is comparable or lower than that of the cement, then the DEM method will not be able to reasonably predict fracture or damage, which in reality should occur in the aggregates as well. This is a major limitation of using such discrete approximations for concrete fracture.

6. Brittle fracture by an elastic projectile

Firstly, we examine impact by a projectile which is perfectly-elastic. Fig. 2 shows the evolution of the stress (left column) and damage (right column) as the projectile collides with the concrete column. The particles are coloured so that the blue-red colour range corresponds to a von Mises stress range of 0 to 250 MPa and damage range of 0 to1.

When the projectile collides at 15.3 ms, the two leading corners of the projectile create very high stresses around the points of contact. Damage initiates from these points and moves horizontally into and across the width of the column. The interaction of the impinging stress waves with the rarefaction compression waves reflected from the opposite vertical face of the column tends to slow the horizontal propagation of damage. So, upon reaching the middle of the column the damage paths turn sideways and propagate vertically to find the fracture plane of lowest strength (along which the fracture will consume the minimum energy), creating a U-shaped

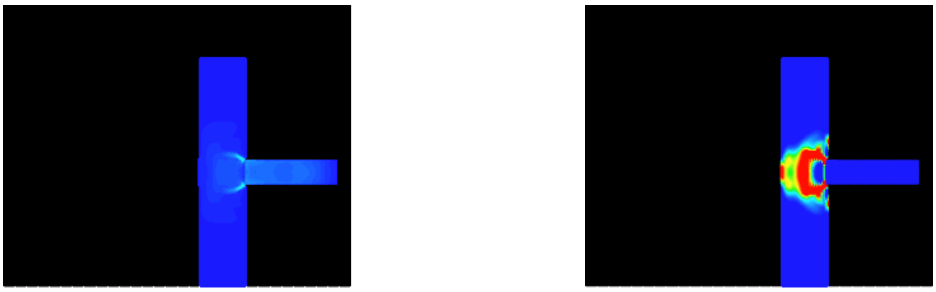

(a) t = 16.5 ms

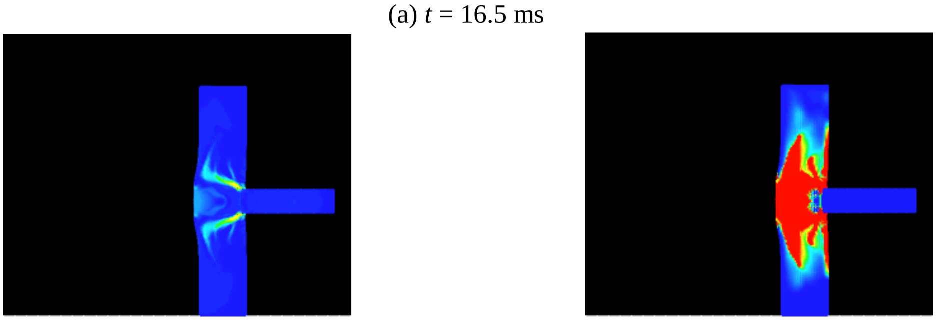

(b) t = 18 ms

Fig. 2 Fracture pattern of the column and fragment distribution after collision for an elastic projectile (left: coloured by von Mises stress (in Pa) and right: coloured by damage)

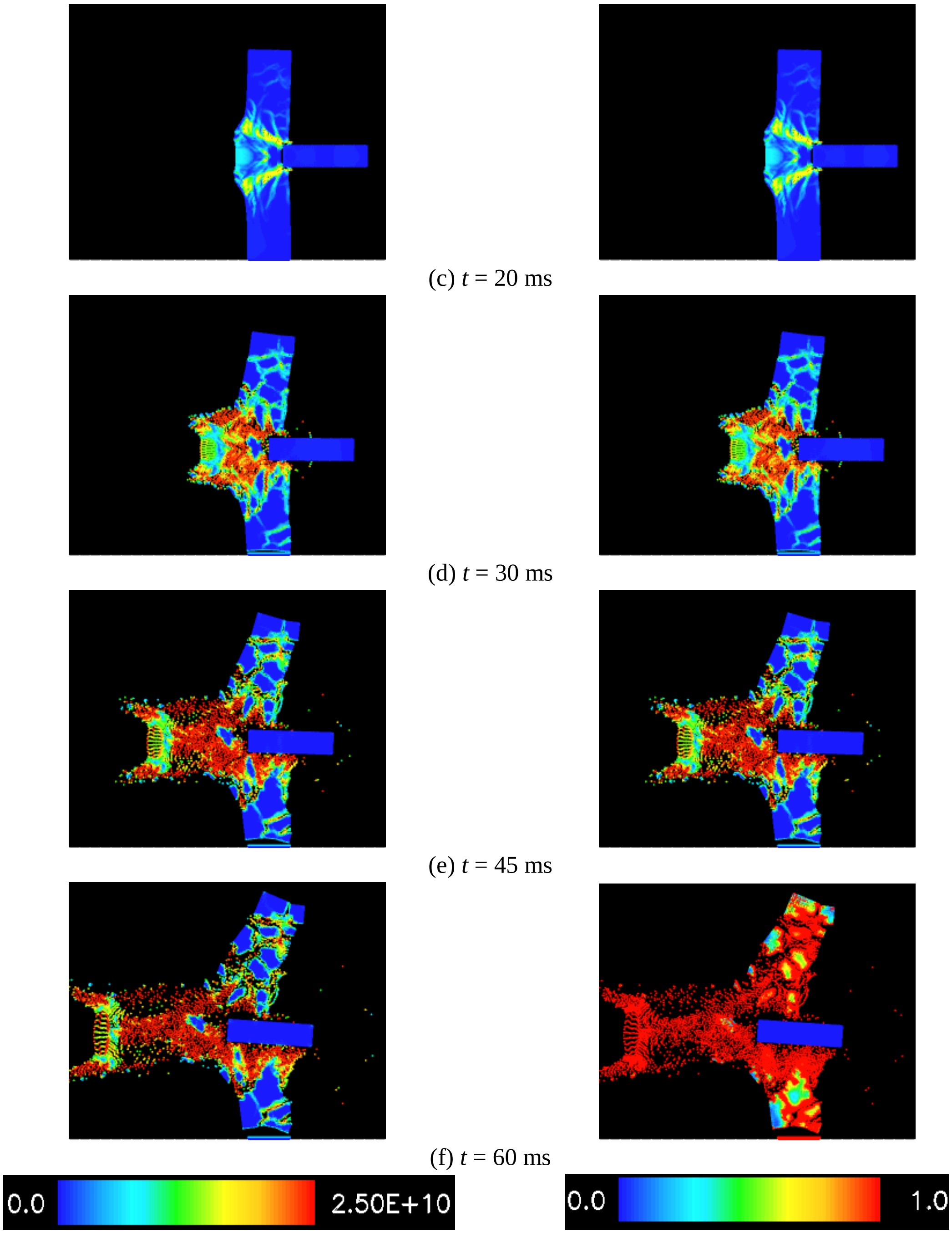

Fig. 2 Continued

fractured zone at 16.5 ms, as seen in Fig. 2(a). Beyond this, a small region of moderate damage is observed on the opposite side of the column due to the reflection of the stress waves.

The early fracture reduces the concrete strength in the region in front of the colliding projectile leading to higher stresses. This region becomes fully damaged by 18 ms, and the damage then propagates vertically in four branches both through the middle of the column and along the impacted surface (Fig. 2(b)). A low stress region accompanied by low damage levels remains in a small area directly in front of the projectile. Fig. 2(c) shows two of the primary vertical (upward) damage paths merging before reaching the top surface. The damage then propagates into the interior and spreads around the top and bottom of the column. Differences in the damage pattern at the top and bottom are observable at 20 ms because of the different boundary conditions at the top and bottom free surfaces. Since the top section of the column is free, it has low stiffness and provides little resistance to fracture development compared to the bottom section which is fixed and has higher stiffness. The damage occurring near the top free surface is therefore more severe.

Fig. 2c shows the onset of fragmentation commencing from the left face of the column. Two distinct regions can be identified based on the level of fragmentation;

- the completely damaged central region with debris/fine particles, and
- the larger fragments above and below this debris zone.

The high central impact stresses lead to an almost fully damaged region in the middle, consisting of a cloud of debris made up of fine materials. The von Mises stress reaches as high as 25 GPa generating these high levels of damage. Paths of high stress lead from the corners of the projectile towards the left face of the column at angles of about 30^0. These broadly correspond to the shape of the pulverised central debris zone marked in Fig. 2(d). The debris cloud erupts horizontally from the left face of the column, leading to its catastrophic failure. The front of the debris cloud is flat with projections near the ends, and the rear is conical in shape due to the inclined primary fracture planes. This shape is related to the frontal shape of the projectile during deformation and the relative dimensions of the target column and the projectile. Fig. 2(d) also shows the separation of the debris cloud from the middle of the column.

Near the top and bottom ends of the column, there are regions of low stress and damage surrounded by cracks indicated by the green stress lines observed in Figs. 2(d)-(e), which demark the secondary fracture planes that become fragmentation boundaries around 30 ms. The stress is extremely low within each fragment, since after fracture no tensile load can be transferred across the cracked regions. The disintegrated particles (debris) subsequently travel in the horizontal direction keeping the frontal shape of the debris unaltered. This leads to catastrophic failure of the column (Fig. 2f). The fragments at the top and bottom do not move appreciably in the horizontal direction.

7. Brittle fracture by an elastoplastic projectile

Next we examine the impact behaviour when the steel projectile is elastoplastic with a yield stress of 250 MPa. As before, the projectile is assumed to have very high damage resistance and so does not undergo fracture. The configuration is otherwise identical to the previous case. Fig. 3 of the projectile where damage is initiated. The damage propagates rapidly to the opposite side of the column, creating a highly fractured region in front of the projectile and extending across most of its width. This early damage distribution is much more uniform and differently shaped than the U-shaped region observed for the perfectly-elastic case (Fig. 2a). The corners of the projectile plastically deform almost immediately upon collision, reducing the initial contact stresses. The resulting lower strain rate reduces and distributes the damage more evenly in front of

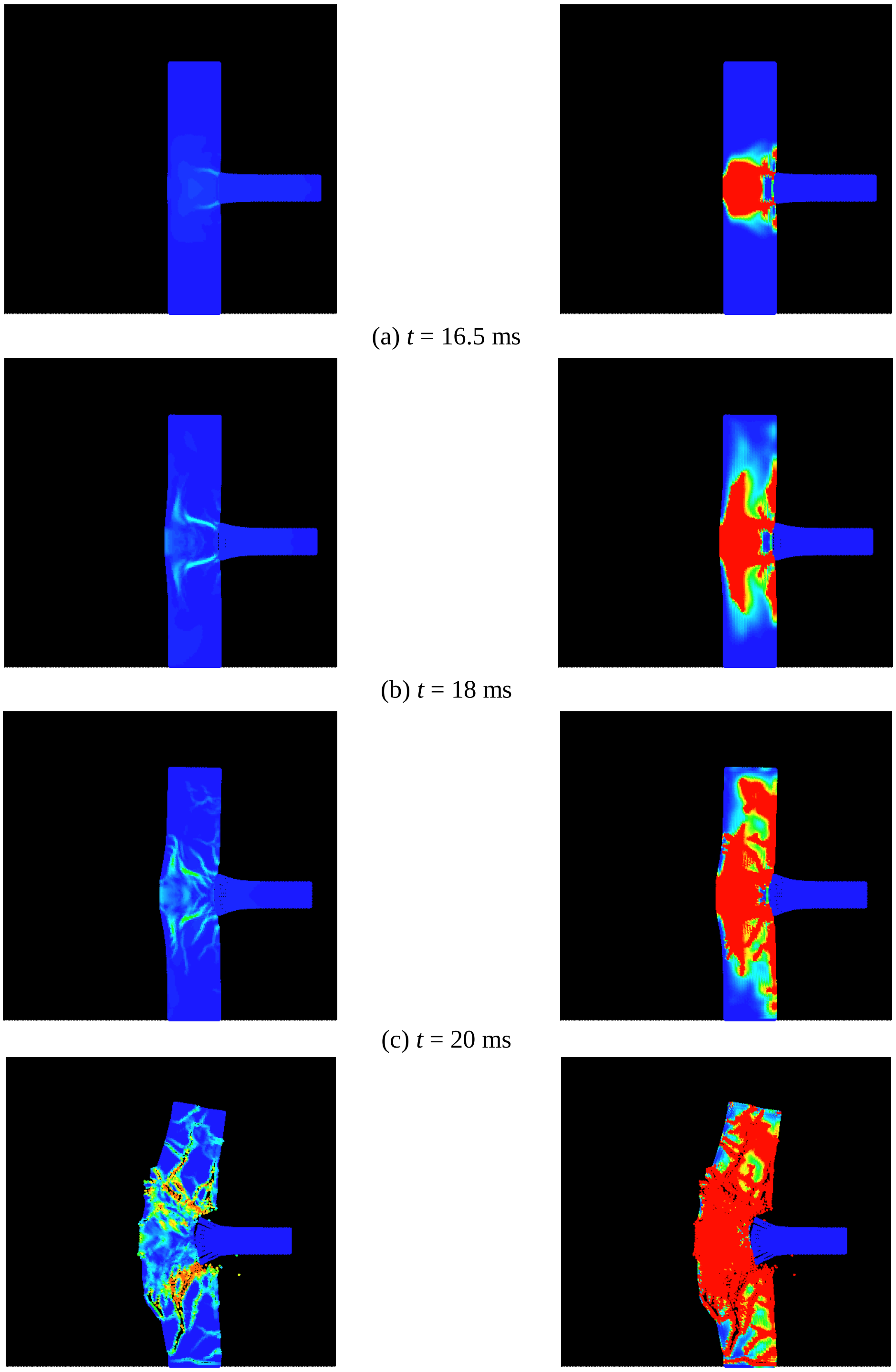

(a) t = 16.5 ms

(b) t = 18 ms

(c) t = 20 ms

(d) t = 30 ms

Fig. 3 Fracture pattern of the column and fragment distribution after collision for an elastoplastic projectile (left: coloured by von Mises stress (in Pa) and right: coloured by damage)

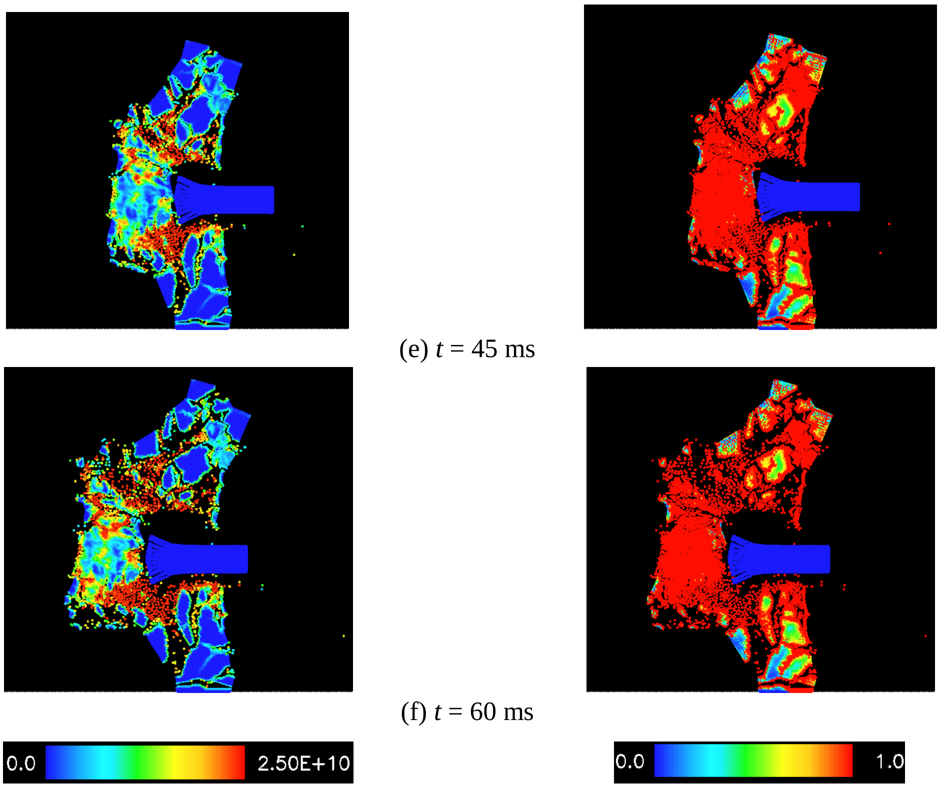

(e) t = 45 ms

(f) t = 60 ms

Fig. 3 Continued

the projectile. After 18 ms (Fig. 3b), the projectile continues to undergo further plastic deformation as it penetrates into the column. The leading face of the projectile now starts deforming considerably resulting in a larger contact area with the column (Fig. 3c). The stresses generated in the column are therefore smaller compared to those for the perfectly-elastic projectile. These lower stresses are unable to produce sharp fracture planes (narrow completely damaged paths), extending through the thickness of the column. Fig. 3d shows that up to 26 ms the high stress zones have not been able to form continuous paths from the right to the left face. As a result, the debris cloud does not erupt from the middle as happens in the perfectly-elastic case. Instead the middle part of the column bulges out towards left, and the upper part tilts towards right.

The fracture pattern is similar at the top and bottom of the column for both the cases. Compared to the perfectly-elastic impact, we observe lower stresses and a more uniform damage distribution in the middle of the column. Unlike the distinct and sharp primary fracture planes observed in the perfectly-elastic impact, the damage is less severe and more widely distributed along the primary fracture planes (Fig. 3e).

The elastoplastic deformation increases the area of contact between the projectile and the column by around 70%. This spreads the impact load over a larger area on the column leading to a lower stresses and also slows the energy transfer from the projectile. This causes the damage to be more evenly distributed in the central region and produces a relatively large debris zone (Fig. 3f). However, for both the cases the fracture pattern at the top and bottom of the column remains essentially the same with further penetration of the projectile. Also for the elastoplastic case, the fragments from the middle of the column travel less distance at the same time compared to the perfectly-elastic impact (Fig. 3f).

Fig. 4 shows the projectile as it contacts the column and undergoes progressive plastic deformation during the collision. Early in the impact (up to 20 ms), the column has suffered only a low level of damage and can offer significant resistance to the motion of the projectile. As a result, the projectile deforms against the column.

The stress at the front of the projectile reaches the yield strength of the material at around 15.5 ms and it starts to plastically deform. By 18 ms, moderate plastic strains of 30-40% at the front of the projectile are observed and it starts to broaden (Fig.4a). By 20 ms, the peak plastic strains have reached 50%, and the front of the projectile has broadened by 50%. This broadening of the face of the projectile spreads the already lower stresses over a larger area, further reducing the stress in this region. The plastic strain reaches a maximum value of 72% at around 22 ms (Fig. 4c) with a corresponding broadening of the face of 70%. As the column then fractures, the force it is able to apply back to the projectile declines rapidly leading to lower stresses in the projectile and a rapidly declining rate of plastic deformation. Any further deformation is elastic and short lived. Fig. 4(d)

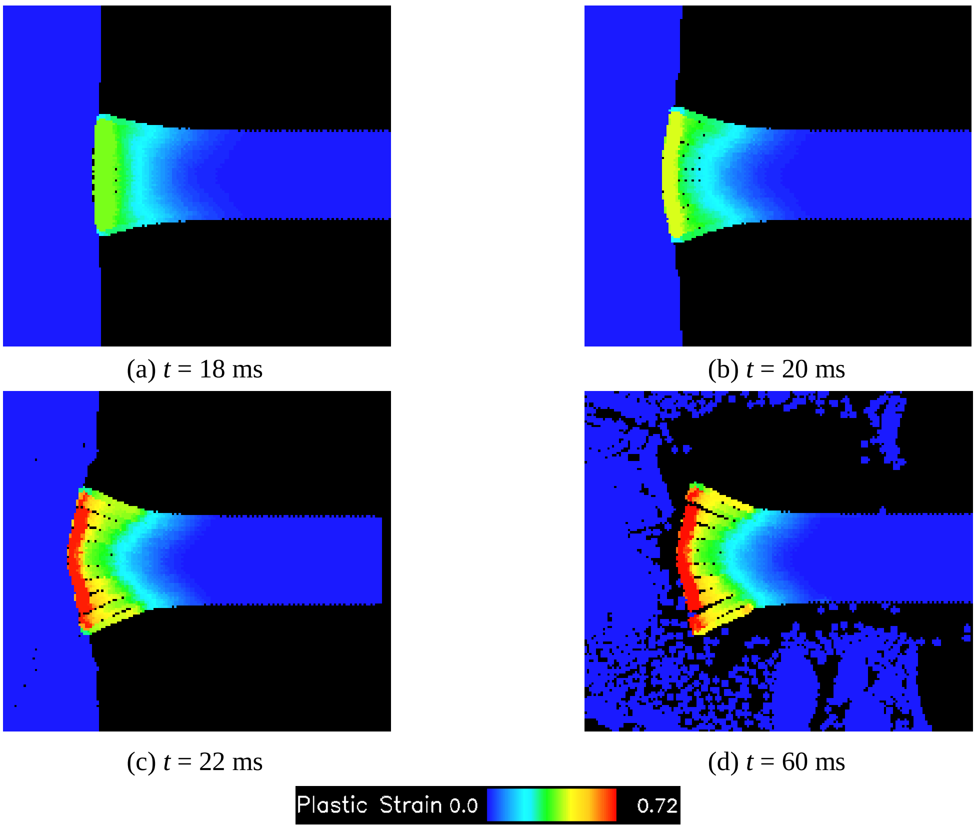

(a) *t* = 18 ms (b) *t* = 20 ms

(c) *t* = 22 ms (d) *t* = 60 ms

Fig. 4 Plastic strain distribution in the elastoplastic projectile during collision

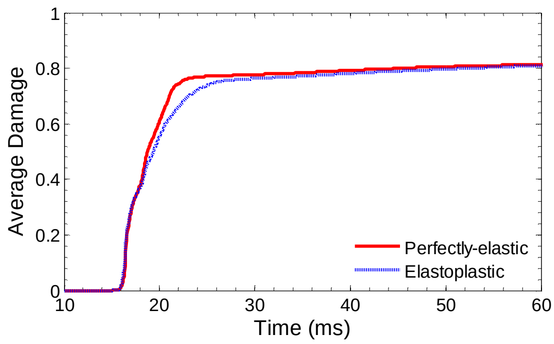

Fig. 5 Variation of average damage in the column with time

shows the final state of the projectile. The plastically strained region is restricted to the leading 1 m of the projectile which is 25% of its length. The highest plastic strains occur in a thin surface layer with a thickness of only 10 cm.

Fig. 5 shows the variation of the total damage of the column during the collision for both the perfectly-elastic and elastoplastic cases. For the perfectly-elastic projectile, the damage commences at 16 ms and rises very sharply until 23 ms. Thereafter, it continues to increase but at a very slow rate. The initial rapid rise in the damage represents the primary and subsequent secondary fracturing of the column.

The slight increase after 23 ms corresponds to the progressive small scale tertiary breakage. For the elastoplastic case, the damage is same up to 18 ms as the projectile deformation is primarily elastic, as seen from the low plastic strain in Fig. 4a. This explains the similar fracture patterns observed in the early stages for both the cases up to 18 ms. However, after 18 ms, the increasing plastic deformation with the accompanying broadening of the front of the projectile (Figs. 4b-c) leads to lower stresses being generated in the column causing the damage to increase more slowly compared to the perfectly-elastic case. When the column is completely fractured, tensile loads can no longer be transmitted between the fragments, and only minor tertiary fracture occurs. The final total amount of damage to the column is very similar for the two cases, but the different breakage paths lead to quite different distributions of the damage, fragmentation patterns in the middle of the column, and debris patterns being ejected.

8. Velocity distribution of the fragments

Fig. 6 compares the velocity distribution of the fragments for the two cases. The particles are coloured by their velocities with dark blue being stationary and red being 217 m/s. The perfectly-elastic projectile produces a velocity distribution that increases from right to left across the column with the material on the extreme left having the highest velocity of around 217 m/s. The velocity progressively decreases for the debris particles towards the interior of the column. The back of the debris cone forms an angle of ~30° due to the inclined fracture planes (Fig. 6(a)). The large damage along the inclined primary fracture planes imparts very high velocities to the debris in these regions creating the projections at the top and bottom of the debris cloud.

For the elastoplastic projectile, the velocity distribution in the debris cloud is markedly more uniform and much lower. The elastoplastic deformation of the projectile has not only reduced the force accelerating the fragments, but also has spread it over a larger area of the column and applied

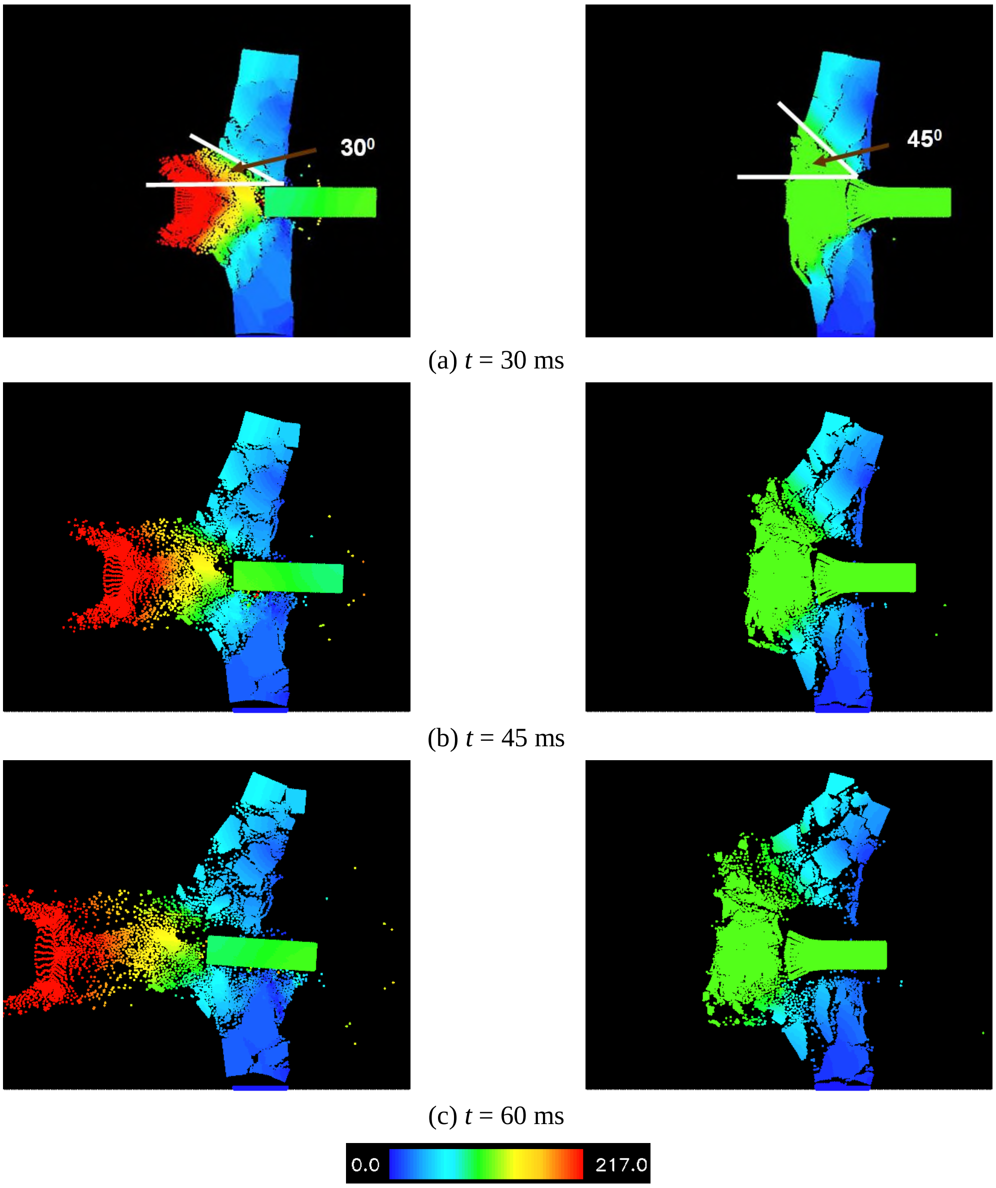

Fig. 6 Comparison of the velocity distribution (in m/s) of the fragments for the elastic (left column) and elastoplastic projectiles (right column)

it for a longer duration. This significantly affects the fracture process and the generation of the debris cloud and its post-impact velocities. The peak fragment cloud velocity is reduced by about 50% to around 109 m/s. A greater uniformity of the fragment velocities causes the front of the debris cloud to be much flatter without any projections of leading fast moving material. The rear angle of the debris cone is also much greater (around 45°) compared to that (around 30°) found for the perfectly-elastic impact.

One key factor that considerably affects the fracture in these collisions is the energy transfer between the colliding bodies. In the elastoplastic case, the energy is transferred at a slower rate but over a longer period. Also, the larger contact area between the projectile and the column reduces the stresses and distributes the transferred energy over a wider region. This changes the fracture pattern and causes the debris fragments to have considerably lower final speeds. However, the speed of the fragments at the top and bottom of the column is not affected much by the nature of the projectile because the early load transmission is similar for both the cases. Before the plastic deformation of the elastoplastic projectile begins to affect the loading, the upper and lower fragments already separate from the middle along the primary fracture planes and further stress transmission is significantly restricted. As a result, the motion of these fragments is almost independent of the subsequent behaviour of the central part of the column.

Fig. 7 shows the variation of kinetic energy of the system (projectile and column) during collision. The kinetic energy remains constant while the projectiles are approaching the column (up to point P). The time required for (primary and secondary) fracture and elastic loading/unloading is indicated by the time over which the change in kinetic energy takes place. The primary fracture occurs in a very short time immediately after the projectile comes in contact with the column.

For the pure elastic case, the projectile undergoes elastic compression and transfers momentum to the column. Part of the initial kinetic energy of the projectile is converted into elastic strain energy of the projectile and part is transferred to the column, and the rest is retained by the projectile as kinetic energy. The kinetic energy loss to the column arises from

- the energy dissipated in fracture,
- the kinetic energy of the accelerated fragments, and
- the elastic energy of the column.

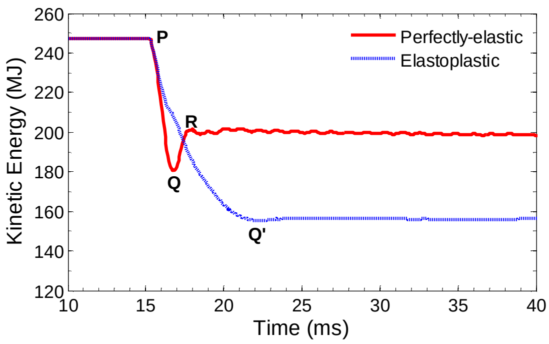

Fig. 7 Variation of the total kinetic energy with time for the perfectly-elastic and elastoplastic cases

However, since the column rapidly undergoes fracture, it stores little elastic strain energy.

The loss of kinetic energy from point P to Q (67 MJ), in Fig. 7, represents the total energy dissipated in fracture and stored in elastic deformation for the elastic projectile case. The elastic unloading of the projectile transfers 21 MJ back into kinetic energy (from point Q to R). Fracturing has ceased by point R, and thereafter the kinetic energy of the bodies (debris cloud, fragments and projectile) remains constant. The difference in kinetic energy between points P and R (46 MJ) represents the energy consumed in fracturing. The time between P and R is the time required for fracture and elastic unloading, which is 2.7 ms.

For the elastoplastic projectile, the energy dissipation also includes a small amount of loss due to plastic deformation. The plastic deformation strongly reduces the rate at which energy is transferred to the column, leading to a longer duration for the primary and secondary fracture of 6.9 ms (a substantial 156% increase). This is consistent with the earlier observation that the slow propagation of fracture for the elastoplastic case allows the damage to be distributed more evenly and produces a larger debris zone (Fig. 6).

In the elastoplastic case, the elastic deformation of the projectile is limited by the yield strength and remains much smaller than that of the elastic case. As a result, there is much less elastic energy stored in the projectile and so there is virtually no recovery of the elastic energy during unloading (as seen by monotonic change of the energy after point Q'). The kinetic energy lost between points P and Q' (90 MJ) is the energy dissipated by the column fracturing and the plastic deformation of the projectile.

The fractions of the initial kinetic energy lost during the collisions are 18% and 37% for the perfectly-elastic and elastoplastic cases respectively. The energy dissipated in fracturing is used in creating new surface area for the fragments. The surface energy depends on the fracture pattern and the size distribution of the fragments. The larger pulverised central region and the smaller fragments produced during the elastoplastic impact possess larger surface area and so consume more energy during fracture. This and the additional energy required for the plastic work lead to the greater loss of kinetic energy in the elastoplastic case.

9. Effect of the material failure strain on the fracture/fragmentation pattern

Many materials exhibit different degrees of "brittleness" depending on their composition, processing conditions during manufacture, and in-service environmental degradation. This is particularly true for concrete. At the preparation stage, the proportion of aggregate to cement, and the size distribution of the aggregates have a major influence on the initial fracture properties. Moreover, during the service life of a concrete structure, the variation in temperature, humidity, moisture and water absorption contributes to progressive degradation of the properties. It is thus of crucial importance to understand how the nature of the fracture pattern varies with the extent of brittleness.

To address this, the effect of the degree of brittleness on the impact induced damage is next studied. A key material property that affects brittle fracture is the failure strain of a material, which is included in the damage model used here via material parameters k and m (see Section 4 for details) that control the threshold failure strain $\varepsilon_{\min}$ (in Eq. 25). The same geometry, impact velocity, material properties (except damage properties) and boundary conditions as those of the base case (given in Section 5) were used in this study. The fracture behaviour of the column was studied with the threshold failure strain of concrete ranging from very small to large values (i.e., 0.001-1.0).

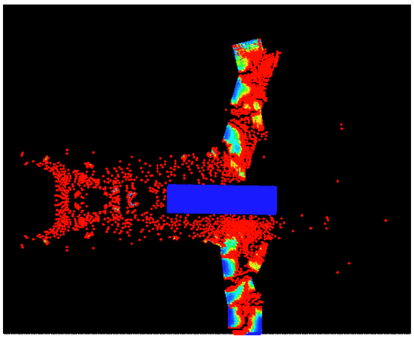

(a) $\varepsilon_{\min} = 0.001$

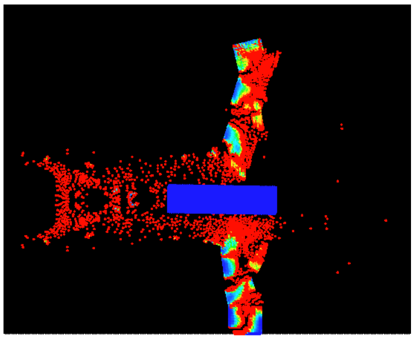

(b) $\varepsilon_{\min} = 0.025$

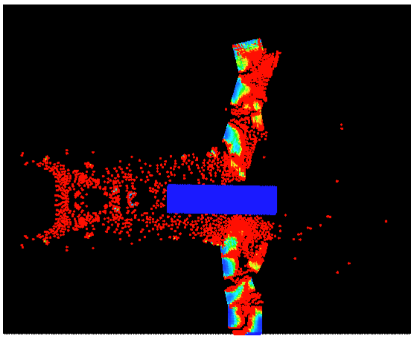

(c) $\varepsilon_{\min} = 0.05$

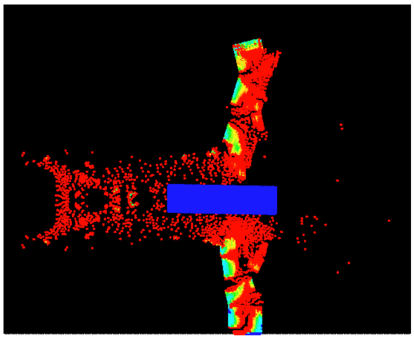

(d) $\varepsilon_{\min} = 0.10$

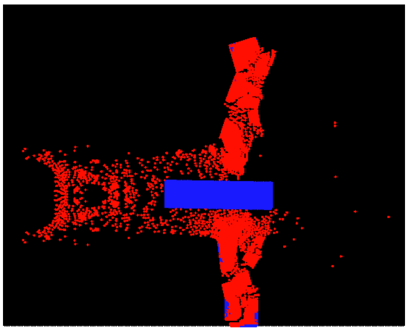

(e) $\varepsilon_{\min} = 0.20$

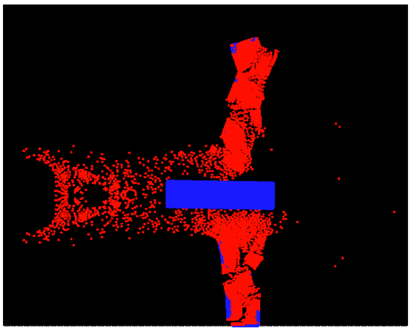

(f) $\varepsilon_{\min} = 0.25$

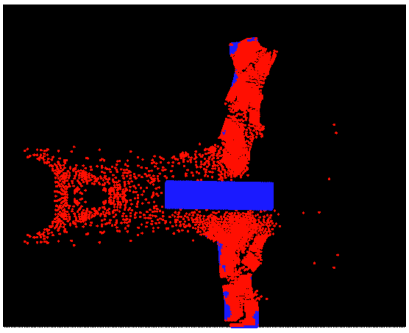

(g) $\varepsilon_{\min} = 0.30$

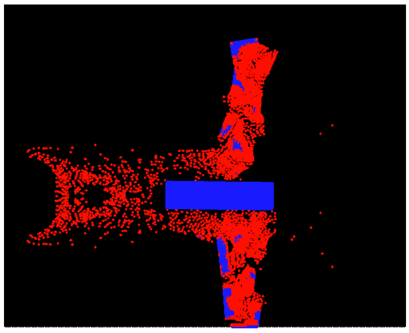

(h) $\varepsilon_{\min} = 0.40$

Fig. 8 Fracture and fragmentation patterns in the column for different threshold failure strains

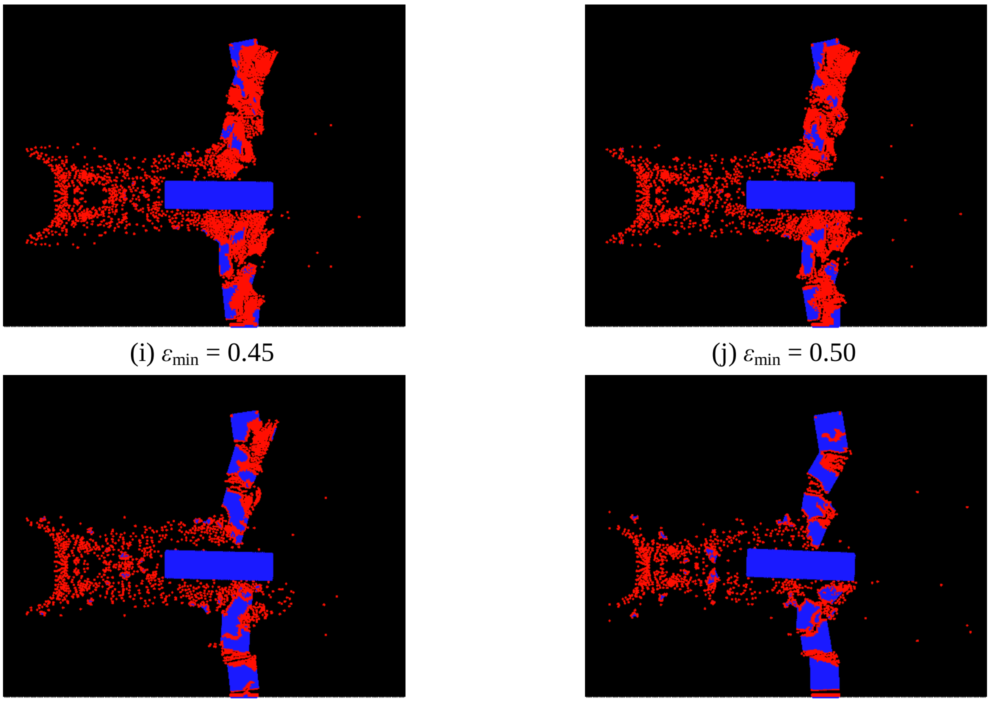

(i) ε_{min} = 0.45 (j) ε_{min} = 0.50

(k) ε_{min} = 0.75 (l) ε_{min} = 1.00

Fig. 8 Continued

Fig. 8 shows the fractured configurations of the column for these cases at 50 ms after the impact. The red and blue colours represent completely damaged and undamaged particles, whereas other colours represent an intermediate level of damage. For all the cases, the concrete column fractures broadly similarly but with locally different levels of damage and varying fragment sizes. The middle portion is severely fractured with the production of a conical debris zone with fragments travelling primarily in the horizontal direction with high velocities. The fractured geometries of the rest of the structure are also mostly similar for all of the cases. However, the degree of damage, as characterised by the damage values of the SPH particles, vary considerably depending on the material threshold strain.

For comparison among the fracture patterns under different threshold failure strains, the degree of damage for a given material is characterised by either it is undamaged (with D = 0), or partially damaged (with $0 < D < 1$), or fully damaged (with D = 1). Based on the level of damage, three different categories of fracture behaviour can be broadly identified for low, medium and high failure strains as follows:

(a) Low strain range: For low threshold strains (for cases with ε_{min} up to 0.10), the fractured structure consists of partially damaged regions (intermediate coloured zones between blue and red) in addition to fully damaged (red) and undamaged (blue) regions. For these cases, before the stresses reach high enough to cause complete damage of the regions away from the initial impact site, these regions are either separated from the main (load bearing) structure or surrounded by completely damaged zones (red zones). Both of these conditions restrict transfer of tensile loads to these regions from the main structure, and as a result the damage levels of the material cannot increase further. This retains partially damaged material at the top and bottom sections of the column (away from the projectile pathway), as observed in Figs. 8(a)-(d). The partially damaged zones decease in size with an increase in the threshold strain.

(b) Medium strain range: For medium threshold strains (for cases with $\varepsilon_{\min} = 0.10$ and $\varepsilon_{\min} = 0.25$), the whole structure is almost fully damaged as shown by the completely damaged (red) SPH particles for the entire column (except at very small regions). For these cases, the generated stresses produce strains that are sufficiently higher than the given threshold values everywhere so as to completely damage the material for the whole structure, as noticed in Figs. 8(e)-(f). There is much more pulverised material, and the fragment sizes are smaller compared to those of the low strain range case.

(c) High strain range: For high threshold strains (for cases with $\varepsilon_{\min}$ equal to or greater than 0.30), the structure is comprised of two regions, fully damaged and undamaged, without any partially damaged region, as shown in Figs. 8(g)-(l). For these cases, the strains generated in some regions never exceed the threshold value prior to the inhibition of load transfer to them due to fragmentation or isolation by fully damaged zones around. Whilst in the remaining regions, the strains become sufficiently high so as to cause complete damage of the material. No partially damaged region is produced in these cases. The proportion of the undamaged regions gradually increases with an increase in the threshold strain, as indicated by the larger blue regions in Fig. 8(g)-(l). For higher failure strains, such as $\varepsilon_{\min} = 0.75$ or $\varepsilon_{\min} = 1.0$, distinct inclined fracture planes and fully damaged areas are found that isolate the undamaged portions of the structure.

From the above, in general, the level of damage at a region depends on the location of that region relative to the initial impact site and the threshold failure strain of the material. These govern whether the intensity of the stress waves will produce sufficient strains so as to cause either complete damage or partial damage or no damage at all before that region is isolated from the main load transferring structure, either by physical separation due to fragmentation or by surrounding fully damaged zones.

10. Conclusions

SPH appears to be well suited to modelling elastic-brittle and elastoplastic-brittle collisions and the resulting fracture. SPH has the advantage of being able to follow very high deformations including self-collision among the fragments (beyond what is possible with the FE and FV methods) due to the absence of any grid structure with any pre-defined connectivity. It naturally keeps track of the material free surfaces generated by fracturing, and thus allows the prediction of the propagation of damage and/or cracks. Upon fracture the motion of the fragments can be tracked naturally because of the Lagrangian nature of SPH. This enables simulation of secondary and tertiary fracture, and the collision of fragments with surrounding objects.

SPH can predict the complex dynamic stresses associated with elastic-brittle or elastoplastic-brittle collisions. This results from the ability of the SPH particles to automatically carry stress and strain history and micro-mechanical properties with them as they move. This potentially allows the incorporation of complex rate dependent constitutive material behaviour and direct prediction of the change in thermo-mechanical properties during fracture.

The projectile-column collision fracture problem studied shows that different material constitutive behaviours (elastic and elastoplastic) of the projectile can produce considerably different fragmentation behaviour in the impacted object even for simple problems. This emphasises that appropriate material models and properties need to be used for numerical modelling of dynamic fracture. The present study shows:

- The von Mises stress distribution obtained is consistent with the fracture pattern observed.
- The very early stress distribution and damage propagation are very similar for both the perfectly-elastic and elastoplastic cases before the stresses have reached the yield strength of the elastoplastic material.
- Over longer times, the perfectly-elastic and elastoplastic cases produce quite different fracture patterns.
- Primary fractures occur along planes inclined at specific angles to the direction of the initial motion of the projectile. This is a typical characteristic of such impacts observed in experiments and real life failures. The inclination angle depends on the nature of projectile material, being around 30° for the perfectly-elastic case and 45° for the elastoplastic case.
- The constitutive behaviour of the projectile (elastic/elastoplastic) is found to have a considerable influence in determining the size distribution and motion of the fragment clouds generated. Upon fracture the middle of the column around the point of impact is pulverised into a cloud of fine debris. The size of the debris zone is much larger for the elastoplastic case due to the relatively slower rate of kinetic energy transfer from the projectile. For the perfectly-elastic case, the debris cloud has a flat front with two projections, and a conical rear shape, whereas it is completely flat in the front and has a greater rear cone angle for the elastoplastic case.
- The elastoplastic projectile generates lower stresses and transfers kinetic energy to the target column at a slower rate compared to the perfectly-elastic case. As a result, the speed of the fragments is lower and more uniform for the elastoplastic case. The fraction of the initial kinetic energy dissipated in a collision with an elastoplastic projectile is considerably greater than that for an elastic projectile due to the higher energy dissipation in fracture and plastic work.
- It was found that the threshold failure strain of the material has a profound effect on the damage suffered by a structure under impact. The local damage at a region of the structure is dependent on its location with respect to the initial impact site and the threshold failure strain. These govern whether the stresses will be high enough to cause either complete damage or partial damage or no damage at all.

References

Aliabadi, M.H. and Rooke, D.P. (1991), *Numerical Fracture Mechanics*, Computational Mechanics Publications and Kluwer Academic Publishers.

Bonet, J. and Kulasegaram, S. (2001), “Remarks on tension instability of Eulerian and Lagrangian corrected smooth particle hydrodynamics (CSPH) methods”, *Int. J. Numer. Meth. Eng.*, **52**(11), 1203-1220.

Cedric, T., Janssen, L.P.B.M. and Pep, E. (2005), “Smoothed particle hydrodynamics model for phase separating fluid mixtures. I. General equations”, *Physical Review E* (Statistical, nonlinear, and soft matter Physics), **72**(1), 016713.

Chen, J.K., Beraun, J.E. and Jih, C.J. (1999), “Improvement for tensile instability in smoothed particle hydrodynamics”, *Comput. Mech.*, **23**(4), 279-287.

Cleary, P.W. (1998), “Modelling confined multi-material heat and mass flows using SPH”, *Appl. Math. Model.*, **22**(12), 981-993.

Cleary, P.W. (2010a), “Elastoplastic deformation during projectile-wall collision”, *Appl. Math. Model.*,

34(2), 266-283.
Cleary, P.W. (2010b), "Extension of SPH to predict feeding, freezing and defect creation in low pressure die casting", *Appl. Math. Model.*, **34**(11), 3189-3201.
Cleary, P.W. and Das, R. (2010a), "The potential for SPH modelling of solid deformation and fracture", *IUTAM symposium on theoretical, Computational and modelling aspects of inelastic media*, B.D. Reddy, Springer Netherlands, Volume 11, pp. 287-296.
Cleary, P.W. and Monaghan, J.J. (1999), "Conduction modelling using smoothed particle hydrodynamics", *J. Comput. Phys.*, **148**(1), 227-264.
Cleary, P., Ha, J., Alguine, V. and Nguyen, T. (2002), "Flow modelling in casting processes", *Appl. Math. Model.*, **26**(2), 171-190.
Cleary, P.W., Ha, J., Prakash, M. and Nguyen, T. (2006a), "3D SPH flow predictions and validation for high pressure die casting of automotive components", *Appl. Math. Model.*, **30**(11), 1406-1427.
Cleary, P.W., Prakash, M. and Ha, J. (2006b), "Novel applications of smoothed particle hydrodynamics (SPH) in metal forming", *J. Mater. Process. Tech.*, **177**(1-3), 41-48.
Cleary, P.W., Prakash, M., Ha, J., Stokes, N. and Scott, C. (2007), "Smooth particle hydrodynamics: status and future potential", *Prog. Comput. Fluid Dy.*, **7**(2-4), 70-90.
Cleary, P.W., Prakash, M., Das, R. and Ha, J. (2012), "Modelling of metal forging using SPH", *Appl. Math. Model.*, **36**(8), 3836-3855.
Das, R. and Cleary, P.W. (2006), "Uniaxial compression test and stress wave propagation modelling using SPH", *Proceedings of the Fifth International Conference on Computational Fluid Dynamics in the Process Industries*. Melbourne, Australia,
Das, R. and Cleary, P.W. (2010), "Effect of rock shapes on brittle fracture using smoothed particle hydrodynamics", *Theor. Appl. Fract. Mec.*, **53**(1), 47-60.
Das, R. and Cleary, P.W. (2013), "A mesh-free approach for fracture modelling of gravity dams under earthquake", *Int. J. Fracture*, **179**(1-2), 9-33.
Das, R. and Cleary, P.W. (2015a), "Evaluation of accuracy and stability of the classical SPH method under uniaxial compression", *J. Sci. Comput.*, **64**(3), 858-897.
Das, R. and Cleary, P.W. (2015b), "Novel application of the mesh-free SPH method for modelling thermo-mechanical responses in arc welding", *Int. J. Mech. Mater. D.*, **11**(3), 337-355.
Davison, L. and Stevens, A.L. (1973), "Thermomechanical constitution of spalling elastic bodies", *J. Appl. Phys.*, **44**(2), 668-674.
Dyka, C.T. and Ingel, R.P. (1995), "An approach for tension instability in smoothed particle hydrodynamics", *Comput. Struct.*, **57**(4), 573-580.
Dyka, C.T., Randles, P.W. and Ingel, R.P. (1997), "Stress points for tension instability in SPH", *Int. J. Numer. Meth. Eng.*, **40**(13), 2325-2341.
Eftekhari, M. and Mohammadi, S. (2015), "Multiscale dynamic fracture behavior of the carbon nanotube reinforced concrete under impact loading", *Int. J. Impact Eng.* [In Press]
Fagan, T., Das, R., Lemiale, V. and Estrin, Y. (2012), "Modelling of equal channel angular pressing using a mesh-free method", *J. Mater. Sci.*, **47**(11), 4514-4519.
Fahrenthold, E.P. and Yew, C.H. (1995), "Hydrocode simulation of hypervelocity impact fragmentation", *Int. J. Impact Eng.*, **17**(1-3), 303-310.
Fang, Z. and Harrison, J.P. (2001), "Numerical analysis of progressive fracture and associated behaviour of mine pillars by use of a local degradation model", *Transactions of the Institution of* Min*ing and Metallurgy, Section A*: Min*ing Industry*, **111**(1), 59-72.
Fang, J., Owens, R.G., Tacher, L. and Parriaux, A. (2006), "A numerical study of the SPH method for simulating transient viscoelastic free surface flows", *J. Non-newton Fluid*, **139**(1-2), 68-84.
Fernandez-Mendez, S., Bonet, J. and Huerta, A. (2005), "Continuous blending of SPH with finite elements", *Comput. Struct.*, **83**(17-18), 1448-1458.
Fujiwara, A. (1989), "Experiments and scaling laws for catastrophic collisions", *Asteroids Ii*, 240-265.
Fujiwara, G. (1994), "Review of fracture mechanics for aircraft structures", Zairyo/*J. Soc. Mater. Sci.*, Japan **43**(493), 1188-1194.

Gingold, R.A. and Monaghan, J.J. (1977), “Smoothed particle hydrodynamics - Theory and application to non-spherical stars”, MNRAS **181**(3), 375-389.

Grady, D.E. and Kipp, M.E. (1980), “Continuum modelling of explosive fracture in oil shale”, *Int. J. Rock Mech.* Min., **17**(3), 147-157.

Grady, D.E., Kipp, M.E. and Smith, C.S. (1980), “Explosive fracture studies on oil shale”, *Soc. Petro. Eng. J.*, **20**(5), 349-356.

Gray, J.P. and Monaghan, J.J. (2004), “Numerical modelling of stress fields and fracture around magma chambers”, *J. Volcanol. Geoth. Res.*, **135**(3), 259-283.

Gray, J.P., Monaghan, J.J. and Swift, R.P. (2001), “SPH elastic dynamics”, *Comput. Method. Appl. M.*, **190**(49-50), 6641-6662.

Harrison, S. and Cleary, P. (2014), “Towards modelling of fluid flow and food breakage by the teeth in the oral cavity using smoothed particle hydrodynamics (SPH)”, *Eur. Food Res. Technol.*, **238**(2), 185-215.

Hu, S., Zhang, X. and Xu, S. (2015), “Effects of loading rates on concrete double-K fracture parameters”, *Eng. Fract. Mech.*, **149**, 58-73.

Huang, Y., Yang, Z., Ren, W., Liu, G. and Zhang, C. (2015), “3D meso-scale fracture modelling and validation of concrete based on in-situ X-ray computed tomography images using damage plasticity model”, *Int. J. Solids. Struct.*, **67-68**, 340-352.

Imaeda, Y. and Inutsuka, S.i. (2002), “Shear flows in smoothed particle hydrodynamics”, *Astrophys. J.*, **569**(1), 501-518.

Ju, J., Jiang, X. and Fu, X. (2007), “Fracture analysis for damaged aircraft fuselage subjected to blast”, *Key Eng. Mater.*, **348-349**, 705-708.

Karekal, S., Das, R., Mosse, L. and Cleary, P.W. (2011), “Application of a mesh-free continuum method for simulation of rock caving processes”, *Int. J. Rock Mech.* Min., **48**(5), 703-711.

Kleine, T., La Pointe, P. and Forsyth, B. (1997), “Realizing the potential of accurate and realistic fracture modeling in mining”, *Int. J. Rock Mech.* Min., **34**(3-4), 661.

Kulasegaram, S., Bonet, J., Lewis, R.W. and Profit, M. (2003), “High pressure die casting simulation using a Lagrangian particle method”, *Commun. Numer. Meth. En.*, **19**(9), 679-687.

Kumar, S. and Barai, S.V. (2010), “Determining the double-K fracture parameters for three-point bending notched concrete beams using weight function”, *Fatigue Fract. Eng. M.*, **33**(10), 645-660.

Lemiale, V., King, P.C., Rudman, M., Prakash, M., Cleary, P.W., Jahedi, M.Z. and Gulizia, S. (2014), “Temperature and strain rate effects in cold spray investigated by smoothed particle hydrodynamics”, *Surf. Coat. Tech.*, **254**, 121-130.

Libersky, L.D. and Petschek, A.G. (1990), “Smooth particle hydrodynamics with strength of materials”, *Advances in the Free-Lagrange Method*, Springer, Berlin, Germany.

Liu, W.K., Jun, S., Li, S., Adee, J. and Belytschko, T. (1995), “Reproducing kernel particle methods for structural dynamics”, *Int. J. Numer. Meth. Eng.*, **38**(10), 1655-1679.

Liu, Z.S., Swaddiwudhipong, S. and Koh, C.G. (2004), “High velocity impact dynamic response of structures using SPH method”, *Int. J. Comput. Eng. Sci.*, **5**(2), 315-326.

Lucy, L.B. (1977), “A numerical approach to the testing of the fission hypothesis”, *Astron. J.*, **82**, 1013-1024.

Melosh, H.J. (1985), “Ejection of rock fragments from planetary bodies”, *Geology*, **13**(2), 144-148.

Melosh, H.J. and Collins, G.S. (2005), “Meteor crater formed by low-velocity impact”, *Nature*, **434**(7030), 157.

Melosh, H.J., Ryan, E.V. and Asphaug, E. (1992), “Dynamic fragmentation in impacts: hydrocode simulation of laboratory impacts”, *J. Geophys. Res.*, **97**(E9), 14735-14759.

Mitchell, R.J. (1993), “Physical modelling of fracture and flow in mine backfills”, *Proceedings of the International Congress on* Mine *Design*, Kingston, ON, Canada, August.

Mok, H., Chiu, W.K., Peng, D., Sowden, M. and Jones, R. (2007), “Rail wheel removal and its implication on track life: a fracture mechanics approach”, *Theor. Appl. Fract. Mec.*, **48**(1), 21-31.

Monaghan, J.J. (1992), “Smoothed particle hydrodynamics”, *Ann. Rev. Astron. Astrophys.*, **30**, 543-574.

Monaghan, J.J. (1994), “Simulating free surface flows with SPH”, *J. Comput. Phys.*, **110**(2), 399-406.

Monaghan, J.J. (2000), “SPH without a tensile instability”, *J. Comput. Phys.*, **159**(2), 290-311.
Monaghan, J.J. (2005), “Smoothed particle hydrodynamics”, *Rep. Prog. Phys.*, **68**, 1703-1759.
Morrison, R.D. and Cleary, P.W. (2004), “Using DEM to model ore breakage within a pilot scale sag mill”, Min*er. Eng.*, **17**(11-12), 1117-1124.
Napier, J.A.L. (1990), “Modelling of fracturing near deep level gold mine excavations using a displacement discontinuity approach”, *International Conference on Mechanics of Jointed and Faulted Rock*, Vienna, Austria
Pierazzo, E. and Melosh, H.J. (2000), “Understanding oblique impacts from experiments, observations, and modeling”, *Ann. Rev. Inc.*, **28**, 141-167, Palo Alto, CA, USA.
Potyondy, D.O. and Cundall, P.A. (2004), “A bonded-particle model for rock”, *Int. J. Rock. Mech.* Min., **41**(8), 1329-1364.
Prakash, M. and Cleary, P. (2015), “Modelling highly deformable metal extrusion using SPH”, *Comput. Particle Mech.*, **2**(1), 19-38.
Randles, P.W. and Libersky, L.D. (2000), “Normalized SPH with stress points”, *Int. J. Numer. Method. Eng.*, **48**(10), 1445-1462.
Rezaie, F. and Farnam, S.M. (2015), “Fracture mechanics analysis of pre-stressed concrete sleepers via investigating crack initiation length”, *Eng. Fail. Anal.*, **58**(Part 1), 267-280.
Selman, E., Ghiami, A. and Alver, N. (2015), “Study of fracture evolution in FRP-strengthened reinforced concrete beam under cyclic load by acoustic emission technique: An integrated mechanical-acoustic energy approach”, *Constr. Build. Mater.*, **95**, 832-841.
Sharir, Y., Stone, D.H. and Pellini, W.S. (1982), “Fracture analysis of cast steel components in rail vehicles”, Gaitherburg, MD, USA, NBS, Washington, DC, USA.
Shockey, D.A., Curran, D.R., Seaman, L., Rosenberg, J.T. and Petersen, C.F. (1974), “Fragmentation of rock under dynamic loads”, *Int. J. Rock Mech.* Min., **11**(8), 303-317.
Skarżyński, Ł., Nitka, M. and Tejchman, J. (2015), “Modelling of concrete fracture at aggregate level using FEM and DEM based on X-ray μCT images of internal structure”, *Eng. Fract. Mech.*, **147**, 13-35.
Swegle, J.W., Hicks, D.L. and Attaway, S.W. (1995), “Smoothed particle hydrodynamics stability analysis”, *J. Comput. Phys.*, **116**(1), 123-134.
Tait, R.B. and Emslie, C. (2005), “The use of fracture mechanics in failure analysis in the offshore diamond mining industry”, *Eng. Fail. Anal.*, **12**(6 SPEC ISS), 893-905.
Takabatake, H., Nonaka, T. and Tanaki, T. (2005), “Numerical study of fracture propagating through column and brace of ashiyahama residential building in Kobe Earthquake”, *Struct. Des. Tall Spec.*, **14**(2), 91-105.
Thorne, B.J., Hommert, P.J. and Brown, B. (1990), “Experimental and computational investigation of the fundamental mechanisms of cratering”, *3rd International Symposium on Rock Fragmentation by Blasting*, Brisbane, Australia.
Uetani, K. and Tagawa, H. (1999), “Earthquake response analysis of steel building frames considering brittle fractures at member-ends”, *Structures Congress* – Proceedings, 406-409.
Vidal, Y., Bonet, J. and Huerta, A. (2007), “Stabilized updated lagrangian corrected SPH for explicit dynamic problems”, *Int. J. Numer. Meth. Eng.*, **69**(13), 2687-2710.
Vignjevic, R., Campbell, J. and Libersky, L. (2000), “A treatment of zero-energy modes in the smoothed particle hydrodynamics method”, *Comput. Method. Appl. M.*, **184**(1), 67-85.
Wang, L., Brust, F.W. and Atluri, S.N. (1997), “Elastic-plastic finite element alternating method (EPFEAM) and the prediction of fracture under WFD conditions in aircraft structures. Part II: Fracture and the T*-integral parameter”, *Comput. Mech.*, **19**(5), 370-379.
Wen, Z., Shiyue, W. and Wancheng, Z. (2005), “The failure and falling of the rock mass in the underground mining”, *Key Eng. Mater.*, **297-300**, 2586-2591.
Wilkins, J.L. (1964), “Calculation of elastic-plastic flow”, *Methods of Computational Physics*, New York, Academic Press, **8**, 211-263.
Wingate, C.A. and Fisher, H.N. (1993), “Strength modeling in SPHC”, Los Alamos National Laboratory.
Yu, K., Yu, J., Lu, Z. and Chen, Q. (2015), “Determination of the softening curve and fracture toughness of

high-strength concrete exposed to high temperature", *Eng. Fract. Mech.*, **149**, 156-169.

CC